Catalysis Letters (2022) 152:315–323
https://doi.org/10.1007/s10562-021-03639-z

Sulfurized Co-Mo Alloy Thin Films as Efficient Electrocatalysts for Hydrogen Evolution Reaction

Cihan Kuru[1,3] · **Mirac Alaf**[1,3] · **Yunus E. Simsek**[2,3] · **Ubeyd Tocoglu**[4]

Received: 19 February 2021 / Accepted: 22 April 2021 / Published online: 28 April 2021

Abstract

Here, we successfully fabricated sulfurized Co-Mo alloy thin film electrodes with different compositions and studied their catalytic properties for hydrogen evolution reaction (HER). The resulting alloy films surpass the HER activity of the MoS_2 counterpart, whose electronic states and morphology are modified by the Co atoms, leading to enhanced HER activity. The best performing electrode at 23 at.% Co concentration exhibits a 272 mV lower overpotential than the MoS_2 film at 10 mA cm^{-2} current density and a Tafel slope of 62 mV dec^{-1}. Combined with the good stability, the sulfurized Co–Mo alloy thin films are promising catalysts for the electrocatalytic HER in acidic solution.

Graphical Abstract

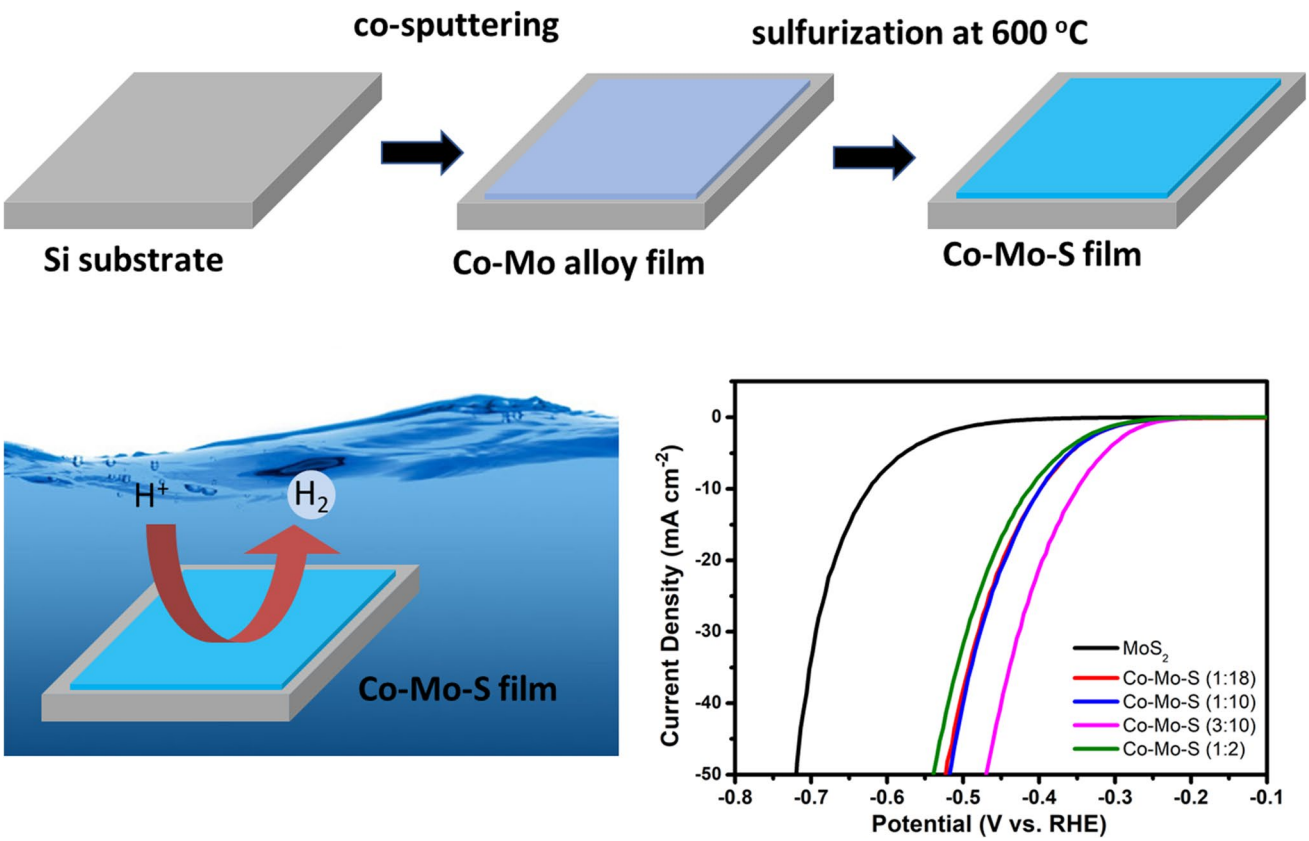

Keywords Hydrogen evolution reaction · Catalyst · MoS_2 · Co · Alloy

Extended author information available on the last page of the article

1 Introduction

Molybdenum disulfide (MoS_2) has been recognized as a promising catalyst to replace Pt for electrochemical hydrogen production [1–5]. The catalytic activity of the MoS_2 stems from the Mo-terminated edges while the basal plane is inert [6]. The basal plane has an S-terminated edge structure with high Gibbs free energy of hydrogen adsorption (ΔG_H), which limits the activity [7]. Many strategies have been devoted to maximize the number of active sites in the MoS_2. Most studies have focused on the preparation of MoS_2 nanostructures with abundant edge sites such as MoS_2 nanoparticles [8, 9], defect rich MoS_2 nanosheets [10, 11], steam vapor etched MoS_2 [12], mechanically distorted MoS_2 nanostructures [13] and MoS_2 aerogels [14, 15]. Another strategy is to insert a third atom into the MoS_2 lattice to form a ternary alloy. Adding a substitutional atom into the MoS_2 modifies the charge distribution at in-plane S sites, which may result in a more favorable ΔG_H value and consequently activation of the basal plane [16]. In addition to the activation of the basal plane, a good electrical conductivity is critical to achieve high HER activity. A solute atom having a different valency than the host atom will induce a doping effect, improving the poor conductivity of the MoS_2 [17]. Various ternary Mo-based sulfides (M–Mo–S, M = Co, Ni, Fe, Cu) have been developed to enhance the electrocatalytic HER activity by exploiting the above-mentioned benefits [18–21]. In a recent study, we reported that Ni addition into MoS_2 thin film leads to a significant improvement in the HER activity [22]. Among the resulting Ni-Mo–S ternary alloy films, the film at 50 at.% Ni concentration was found to exhibit the highest activity. Similar promotional effect of Co has been observed in HER. For example, Dai et al. used a facile deposition–precipitation method to synthesize few layered Co-doped MoS_2 on carbon black [23]. Co atoms were found to substitute Mo, leading to an edge terminated hexagonal structure, which is desirable to expose more edge sites. In addition, Co modified the electronic structure of MoS_2 to lower the ΔG_H of the Mo–S edges from 0.18 to 0.10 eV, improving the hydrogen adsorption. A superior catalytic activity was reported for the Co-doped MoS_2 at Co:Mo = 0.2 molar ratio.

In this study, we systematically investigate the effect of Co addition on the catalytic properties of the sulfurized Co–Mo alloy thin films for electrocatalytic hydrogen production. Co–Mo alloy films having different Co:Mo atomic ratios were deposited with a good compositional control and uniformity by magnetron sputtering and subjected to a thermal sulfurization process. A thin film geometry was used for the catalysts to determine the intrinsic activity by mitigating the morphological effects on the HER performance. The physical and chemical properties of the films were studied by X-ray diffraction (XRD), scanning electron microscopy (SEM), energy dispersive X-ray spectroscopy (EDX), X-ray photoelectron spectroscopy (XPS) and Raman spectroscopy. The HER performance of the catalyst films was evaluated by electrochemical measurements, which indicated that sulfurized Co-Mo alloy films exhibit markedly higher HER activity compared to MoS_2.

2 Experimental Methods

2.1 Sputter Deposition of the Co–Mo Alloy Films

Prior to deposition, Si substrates were cleaned in acetone and isopropyl alcohol using an ultrasonic bath and subsequently the native oxide layer was removed in diluted HF, followed by rinsing in DI water and drying with N_2 blow. 20 nm thick Co–Mo alloy films having varying amounts of Co were deposited on n^+ Si (100) substrates by simultaneously sputtering Mo (99.9% purity, Kurt Lesker) in DC mode and Co (99.9% purity, Kurt Lesker) in AC mode in a multi-target magnetron sputtering system (Vaksis Angora). The base pressure of the sputter chamber was 5×10^{-6} Torr. The Co:Mo atomic ratio in the alloy films was adjusted to 1:18, 1:10, 3:10 and 1:2 by changing the sputter power of Mo target (See the supplementary material for the details.). The sputtering process was carried out with Ar gas having a pressure of 10 mTorr. To avoid the cross-contamination, targets were cleaned at each run by pre-sputtering for 5 min while shutter was closed. The substrate holder was rotated at 5 rpm to improve the compositional and thickness uniformity.

2.2 Thermal Sulfurization of the Co–Mo Alloy Films

The thermal sulfurization of the Co–Mo alloy films were conducted under atmospheric pressure in a tube furnace (MTI OTF-1200X-S-NT-LD), in which a 2 inch diameter quartz tube is horizontally mounted. The samples were positioned at the center of the tube whereas 0.5 g sulfur powder (Merck Millipore) at the upstream side. The tube was flushed with high purity N_2 gas (99.999% purity) for 60 min, then the furnace was gradually heated to 600 ℃ with a rate of 10 ℃/min and kept there for 20 min before cooled to room temperature naturally. N_2 gas flow at 100 s.c.c.m flow rate was maintained during the whole process. When the furnace temperature reaches 600 ℃, the sulfur powder is heated to above its melting temperature (150 ℃) to produce a vapor, which is carried to the samples by the Ar gas. The sulfurized Co:Mo alloys with 1:18, 1:10, 3:10 and 1:2 atomic ratios are denoted as Co–Mo–S (1:18), Co–Mo–S (1:10), Co–Mo–S (3:10) and Co–Mo–S (1:2), respectively.

2.3 Characterization

Grazing angle XRD measurements were performed on Rigaku D-Max diffractometer using a Cu-Kα source (1.54 Å). SEM and EDX analysis were carried out with FEI Quanta FEG 450 scanning electron microscope. XPS data were obtained using SPECS FlexMod spectrometer. The samples were excited by Al-Kα radiation source with photon energy of 1486.71 eV. Binding energies were calibrated with respect to the C 1 s peak (284.8 eV) of adventitious carbon. Raman spectroscopy measurements were conducted by WITech alpha 300R spectrometer with an excitation wavelength of 532 nm at 5 mW.

2.4 Electrochemical Measurements

The working electrodes were prepared as the following: the backside of the Si substrates were scratched using a diamond scriber to remove native oxide layer and then a piece of Cu wire was attached using silver epoxy. Finally, chemically resistant epoxy (Hysol 3423) was applied to define an active area ranging from 0.2 to 0.5 cm^2 on the front side of the samples. The active area of the samples was determined using Imagej software. Electrochemical measurements were conducted with Gamry Interface 1000 potentiostat in a three-electrode setup consisting of a working electrode, Ag/AgCl reference electrode and Pt coil counter electrode. The solution was purged with N_2 and stirred at 750 rpm during the measurements. Linear sweep voltammetry (LSV) measurements were conducted between 0 and (− 0.8) V vs. Ag/AgCl with a scan rate of 5 mV s^{-1}. The LSV data were IR-corrected. Impedance data were taken at the overpotential of 400 mV over a frequency range of 0.1 Hz to 1 MHz. The amplitude of the excitation voltage was 5 mV. The Ag/AgCl potential was converted to reversible hydrogen electrode (RHE) potential using the relation: E(RHE) = E(Ag/AgCl) + 0.059 pH + 0.209 V. The stability of the samples were assessed by comparing the polarization curves taken before and after 1000 cycles of CV scans performed from − 0.2 to − 0.6 V vs. Ag/AgCl with a scan rate of 50 mV s^{-1}. To determine the double layer capacitance (C_{dl}), multiple CV scans were recorded in the potential range of 0.1–0.3 V vs. RHE with the scan rates of 20, 40, 60, 80 and 100 mV s^{-1}.

3 Results and Discussions

Figure 1a presents the XRD patterns of sulfurized Mo, Co and Co–Mo alloy thin films. The sulfurized Mo film exhibits peaks at 13.75°, 33.04°, 33.52° and 58.59°, corresponding to the (002), (100), (101) and (110) planes of hexagonal MoS_2 (PDF#01-075-1539). The peaks observed in the patterns of

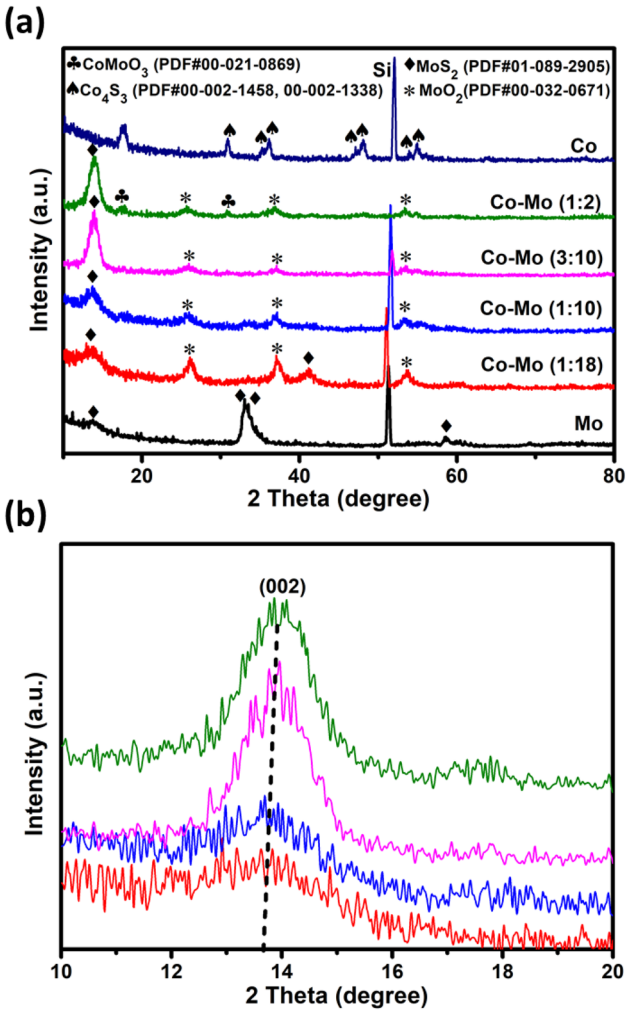

Fig. 1 **a** XRD patterns of the sulfurized Mo, Co and Co–Mo alloy films. **b** Close-up of the (002) peak of the sulfurized Co–Mo alloy films

the sulfurized Co-Mo alloy films arise from both MoS_2 and MoO_2 (PDF#00-032-0671) phases. As the Co atomic ratio is increased in the film, the (002) peak of the MoS_2 phase becomes sharper and taller whereas the MoO_2 related peaks get weaker, indicating that Co promotes the growth of the MoS_2 phase. Moreover, the position of the (002) peak shifts from 13.75° to 13.95°, suggesting the reduction of the interlayer spacing (Fig. 1b). The sulfurized Co-Mo (1:2) film shows additional peaks, which were assigned to $CoMoO_3$ (PDF#00-021-0869). No cobalt sulfide phases could be detected in the alloy films, implying that Co was successfully incorporated into the MoS_2 lattice. On the other hand, the sulfurized Co film displays diffraction peaks, which match well with Co_4S_3 (PDF#00-002-1458, 00-002-1338).

The morphology of the MoS_2 and Co–Mo–S (3:10) films are compared in Fig. 2a and b. The MoS_2 film has a smooth surface with no distinctive features while nanoparticle-like

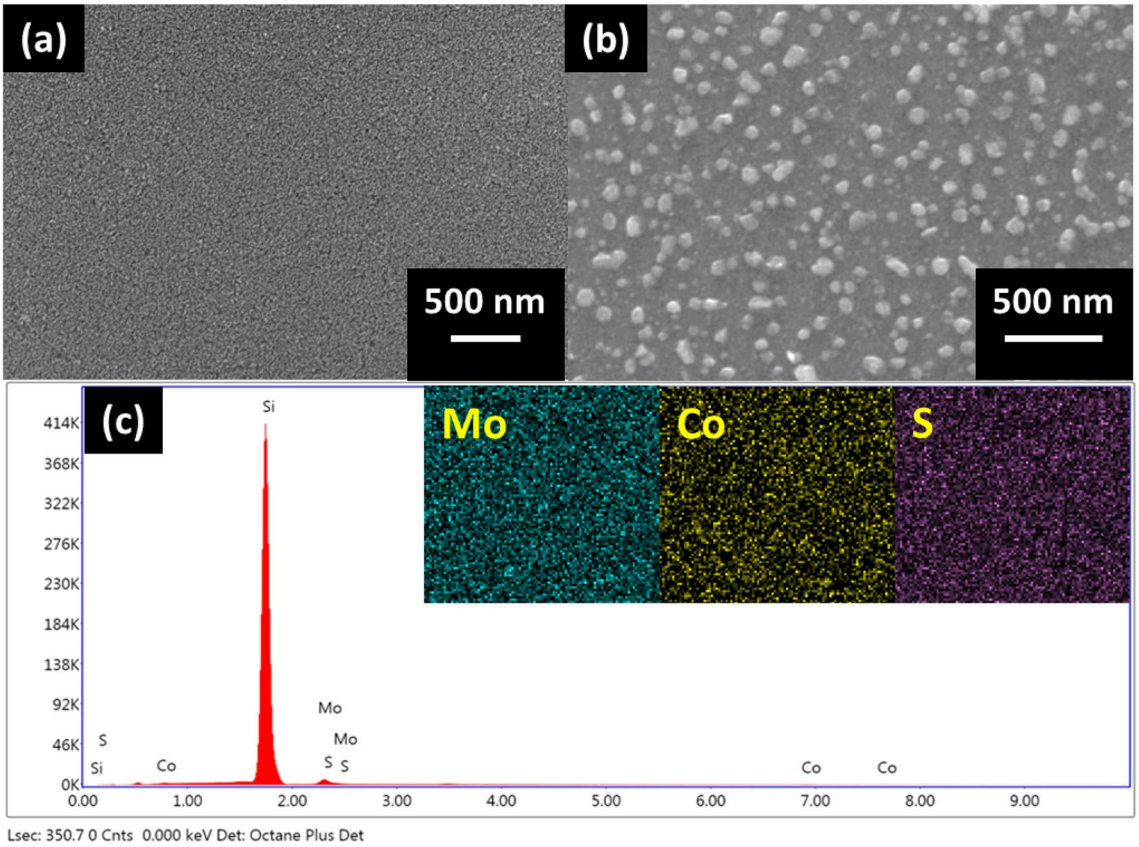

Fig. 2 SEM images of the **a** MoS_2 and **b** Co–Mo–S (3:10) films. **c** EDX spectrum of the Co–Mo–S (3:10) film. (*Inset* shows the EDX mapping results for Co, Mo and S elements.)

formations are scattered on the surface of the Co–Mo–S (3:10) film. Other Co–Mo–S thin films were found to exhibit similar morphologies as well (Fig. S2). However, the particle size is much larger in the Co–Mo–S (1:2) film compared to others. On the other hand, The EDX spectrum of the Co–Mo–S (3:10) film (Fig. 2c) shows the Co, Mo and S peaks, confirming the composition of the sample. Note that the Si peak is originated from the substrate. Furthermore, the EDX mapping analysis (inset of Fig. 2c) indicates the uniform elemental distribution of Co, Mo and S.

XPS measurements were performed to verify the composition of the catalyst films and identify the oxidation states of the elements. The survey scans recorded from 0 to 900 eV reveals the presence of Mo, S, O and C elements for both MoS_2 and Co–Mo–S (3:10) films (Fig. 3a). Aside from that, an additional peak arising from Co was detected in the Co–Mo–S (3:10) film. The atomic ratio of the Co to Mo was measured to be 3:9, which is close to the theoretically calculated value of 3:10. Figure 3b shows the high resolution XPS spectra of Mo 3d for the MoS_2 and Co–Mo–S (3:10) films. The MoS_2 film exhibits doublets at 229.6 and 232.8 eV, which can be assigned to Mo^{+4} oxidation state [24]. In addition, the vague peak observed at 236.1 eV corresponds to Mo^{+6} [25] whereas the peak at 226.8 eV is originated from the S 2p orbitals [26]. The same doublets appear at 228.5 and 231.6 eV for the Co–Mo–S (3:10), which translates to a redshift of 1.1–1.2 eV. The XPS spectrum of Co 2p region (Fig. 3c) in the Co–Mo–S (3:10) film exhibits two sets of Co $2p_{3/2}$ and Co $2p_{1/2}$ doublets located at 781.7/797.1 and 778.5/793.5 eV, reflecting the Co^{+2} oxidation state in Co-S bonds [27] and Co^0 state in Co–Co bonds [28], respectively. Moreover, two satellite peaks are detected at the binding energies of 786.1 and 802.3 eV. The S 2p spectra (Fig. 3d) can be deconvuluted to S $2p_{3/2}$ and S $2p_{1/2}$ doublets, which are centered at 162.4 and 163.6 eV for the MoS_2 film, revealing the − 2 oxidation state of sulfur in the MoS_2 [29]. The peaks shift to 161.2 and 162.4 eV in the case of Co–Mo–S (3:10) film, indicating a lower oxidation state. The XPS results clearly demonstrate that the electronic structure of the MoS_2 is modulated by the Co addition.

Raman spectroscopy measurements were performed to further probe the structural changes in the MoS_2 film after Co incorporation. The Raman spectra of the MoS_2, Co–Mo–S (3:10) and Co–Mo–S (1:2) films are shown in Fig. 4, in which all three samples exhibit the characteristic E^1_{2g} and A_{1g} peaks of MoS_2 [30], indicating that MoS_2 crystal

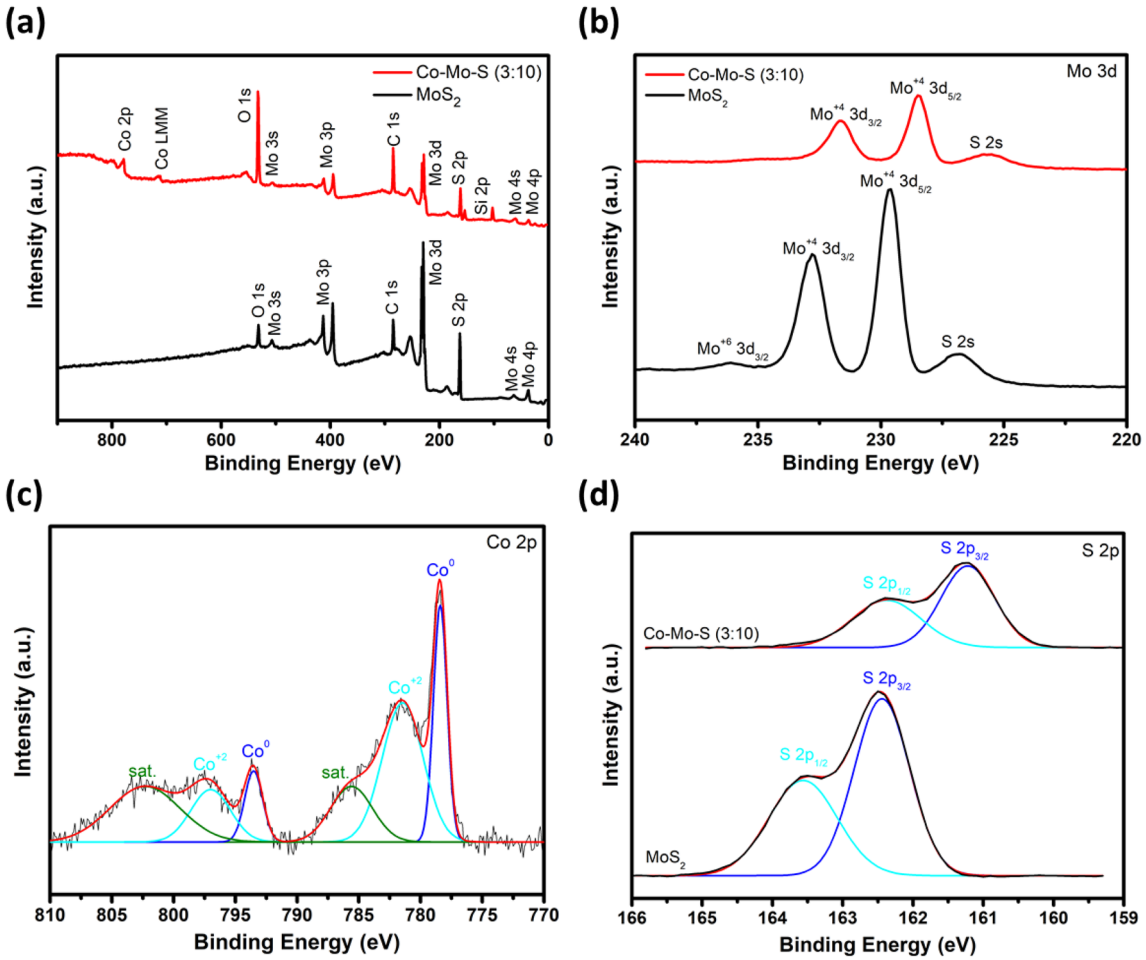

Fig. 3 **a** XPS survey spectra of the MoS_2 and Co–Mo–S (3:10) films. The high-resolution **b** Mo 3d spectra of the MoS_2 and Co–Mo–S (3:10) films, **c** Co 2p spectrum of the Co–Mo–S (3:10) film and **d** S 2p spectra of the MoS_2 and Co–Mo–S (3:10) films

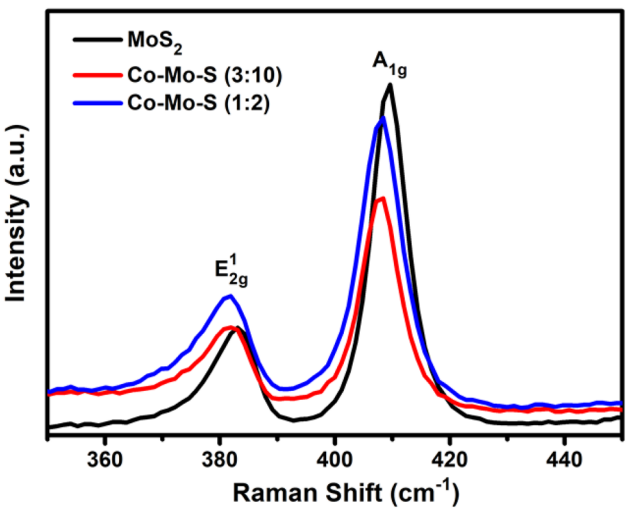

Fig. 4 Raman spectra of the MoS_2, Co–Mo–S (3:10) and Co–Mo–S (1:2) films

structure was maintained after Co incorporation. No Co–S related vibrational modes could be detected, confirming the substitutional Co doping in the MoS_2. Furthermore, the Raman peaks of the Co–Mo–S alloy films display a downward shift relative to the MoS_2 as a result of the increasing electron concentration, suggesting n type doping [31]. Such doping is beneficial for HER because it will improve the poor electrical conductivity of the MoS_2. The E^1_{2g} and A_{1g} peaks are resulted from the in-plane and out-of-plane vibration modes of Mo–S bonds, respectively [32]. MoS_2 layers can be stacked vertically or horizontally or a mixed stacking may occur. In a horizontally stacked MoS_2, the surface is terminated with the terrace sides whereas in vertically a stacked MoS_2 it is terminated with the edge sides. For the terrace terminated MoS_2, the intensity of the E^1_{2g} is comparable to that of A_{1g} [33]. However, as the intensity of the E^1_{2g} peak is considerably smaller compared to A_{1g} in the MoS_2 and Co–Mo–S films we can infer that the films have a mixed structure of terrace and edge termination. The intensity ratio

of the E^1_{2g} to A_{1g} provides information regarding the degree of edge termination in the MoS_2 [33]. The ratio increases from 0.28 to 0.33 with Co addition, pointing out less edge termination in the Co–Mo–S films compared to MoS_2. This is also consistent with the increasing intensity of the (002) diffraction peak with increasing Co concentration.

The HER activities of the catalyst thin films were assessed in 0.5 M H_2SO_4 solution using LSV measurements. The resulting polarization curves are shown in Fig. 5a, in which the Co–Mo–S alloy films have larger current densities at lower overpotentials compared to the MoS_2, indicating superior catalytic activity. The HER performance parameters of the catalyst films are summarized in Table 1. Among the Co–Mo–S alloy films, the Co–Mo–S (3:10) exhibits the highest catalytic activity with an overpotential of 352 mV to attain 10 mA cm^{-2} current density, which is 272 mV smaller than that of the MoS_2. When the Co:Mo ratio is increased to 1:2 the HER performance degrades, revealing that 3:10 is the optimum ratio. This may be due to the appearance of the $CoMoO_3$ phase in the Co–Mo–S (1:2) film as indicated by the XRD results. The HER performance of the Co_4S_3 electrode was also tested, which showed decreasing activity

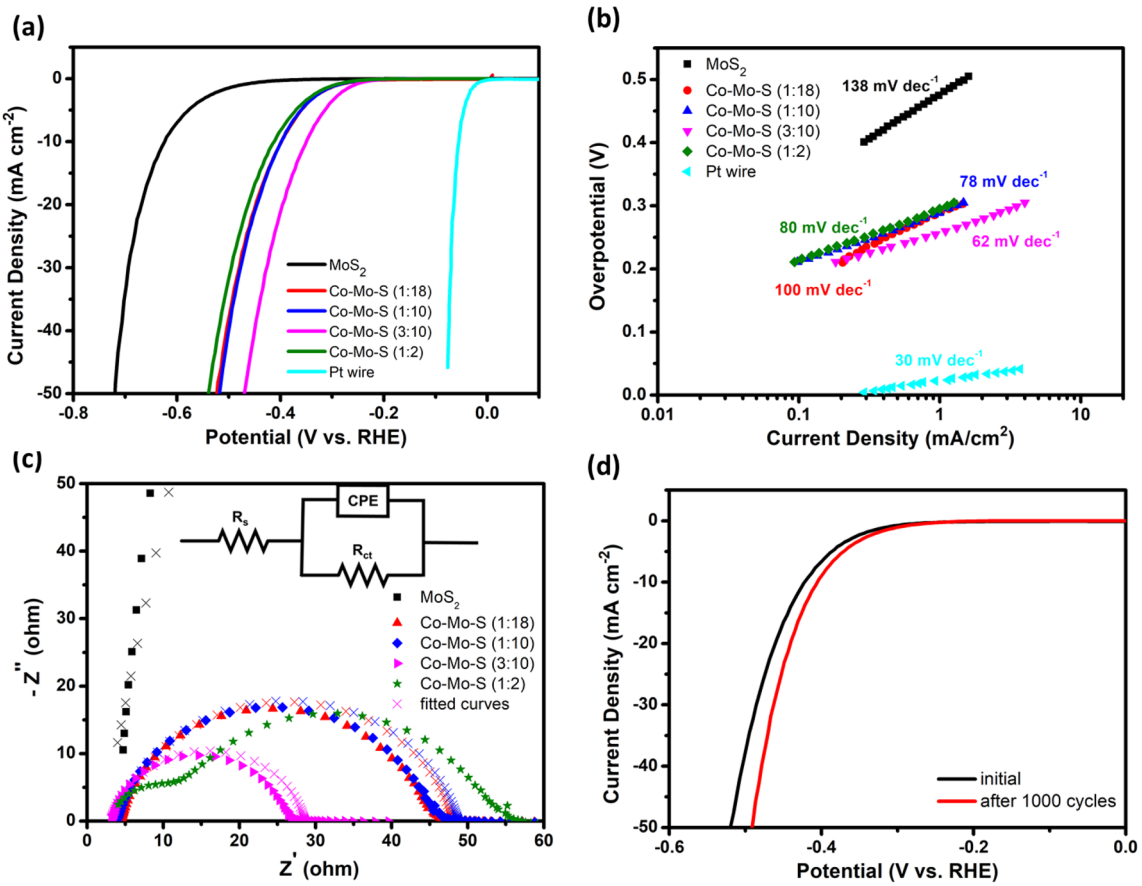

Fig. 5 **a** Polarization curves and **b** Tafel plots of the MoS_2, Pt wire and Co–Mo–S alloy films. **c** Nyquist plots of the MoS_2, and Co–Mo–S alloy films. **d** Stability test result of the Co–Mo–S (3:10) electrode

Table 1 Electrochemical HER performance parameters of the catalyst films

Catalyst	Overpotential @ 10 mA cm^{-2} (mV)	Tafel slope (mV dec^{-1})	R_{ct} (ohm)	C_{dl} (μF cm^{-2})
MoS_2	624	138	10,000	9
Co–Mo–S (1:18)	400	100	44	50
Co–Mo–S (1:10)	400	78	45	47
Co–Mo–S (3:10)	352	62	25	48
Co–Mo–S (1:2)	416	80	48	67

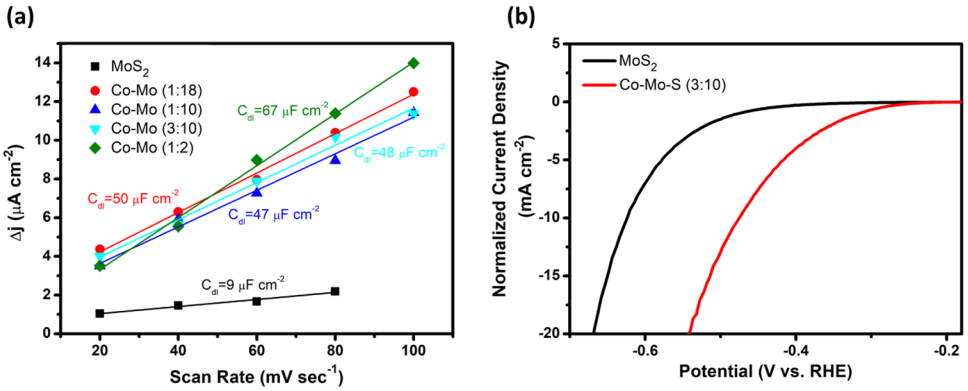

Fig. 6 **a** Estimation of the double layer capacitance of the catalyst films. **b** The comparison of the polarization curve of the MoS_2 film and the normalized polarization curve of the Co–Mo–S (3:10) film by its relative double layer capacitance value to the MoS_2

at the consecutive LSV measurements (Fig. S3), manifesting its poor stability.

Tafel slopes were obtained from the plots of the overpotential vs. the logarithm of current density to determine the HER mechanism of the catalyst films (Fig. 5b). The Tafel slope of the MoS_2 film is 138 mV/dec, which implies the Volmer-Heyrovsky reaction mechanism with the rate determining step of hydrogen adsorption [34]. The slope values of the Co–Mo–S alloy films ranging from 62 to 100 mV dec^{-1} suggest the same reaction mechanism with improved hydrogen adsorption behavior. The Co–Mo–S (3:10) film exhibits the smallest slope value of 62 mV dec^{-1}, indicating a transition to the rate determining step of hydrogen desorption [35]. The adsorption of the H^+ ions on the basal plane of the MoS_2 is limited due to the high ΔG_H value of the in-plane sulfur sites, which dramatically lowers the overall catalytic activity [7]. As the Co atoms are introduced into the MoS_2 lattice, the charge distribution of the sulfur is affected. The XPS results indicated that the sulfur atoms in the Co–Mo–S (3:10) film hold more negative charge compared to the MoS_2, thereby facilitating the adsorption of H^+ ions and consequently boosting the HER performance. Moreover, we speculate that the granular morphology of the Co–Mo–S alloy films may also play a role in the enhanced HER activity. A geometrical constraint is imposed on the surface atoms by the curvature of the spherical nano-grains, which could modify the ΔG_H of the in-plane sulfur atoms [36].

Electrochemical impedance spectroscopy measurements were conducted at 400 mV overpotential to study the reaction kinetics of the catalyst films. All Nyquist plots except for the Co–Mo–S (1:2) (Fig. 5c) exhibit single semicircles that could be best fitted to a CPE-modified Randle's model (inset of Fig. 5c), in which R_s is the solution resistance, R_{ct} is the charge transfer resistance and CPE is the constant phase element. The fittings yielded R_{ct} values of 10 kohm, 44 Ω, 45 Ω and 25 Ω for the MoS_2, Co–Mo–S (1:18), Co–Mo–S (1:10) and Co–Mo–S (3:10), respectively. On the other hand, the Co–Mo–S (1:2) film features two semicircles, which could be due to the additional $CoMoO_3$ phase observed in the sample. The semicircle in the low frequency region was used for the fitting, which gave a R_{ct} value of 48 Ω. The Co–Mo–S alloy films exhibit much lower R_{ct} than MoS_2, indicating faster reaction rates [37]. The Co reduces the R_{ct} of the MoS_2 by improving its charge transport ability as well facilitating charge transfer at the electrode/electrolyte interface. Moreover, the lowest R_{ct} value of the Co–Mo–S (3:10) film correlates with its highest activity.

For practical applications, catalysts are required to have long-term stability in acidic solutions. The stability of the best performing electrode was assessed by comparing the polarization curves taken before and after 1000 CV cycles (Fig. 5d). The electrode shows no sign of degradation after the test, revealing the good stability of the catalyst film. We performed Raman spectroscopy measurements to further evaluate the stability of the Co–Mo–S (3:10) film. Fig. S4 compares the Raman spectra of the film taken before and after 1000 cycles of CV scans. The Raman spectra of the catalyst film shows no significant change after the CV scans, indicating the structural stability of the film.

The incorporation of Co into the MoS_2 obviously changes the morphology, resulting in an increased roughness as presented by the SEM images. To evaluate the effect of morphology on the electrochemical surface area (ECSA), double layer capacitance (C_{dl}) was obtained from the slope of the Δj vs. scan rate plot (Fig. 6a), where Δj stands for the capacitive current density difference of the forward and backwards CV scans at 0.15 V vs. RHE. As the C_{dl} is proportional to the ECSA [38], the C_{dl} values of the electrodes can be used for comparison. The Co–Mo–S alloy films have comparable C_{dl} values (47–67 μF cm^{-2}) whereas the C_{dl} of the MoS_2 film (9 μF cm^{-2}) is significantly lower. This is consistent with the observed flat surface of the MoS_2 film. The intrinsic activity of the MoS_2 and Co–Mo–S (3:10) films was compared through normalizing the polarization curve of the Co–Mo–S (3:10) by its relative C_{dl} to the MoS_2 film. Hence, the effect of variations in the ECSA could be excluded. The normalized curves are displayed in Fig. 6b, in which the Co–Mo–S (3:10) film requires 474 mV to achieve

10 mA cm^{-2} current density, which is still 150 mV lower than the MoS_2. This result clearly shows that the intrinsic activity of the Co–Mo–S (3:10) catalyst film is notably higher than the MoS_2 due to the promotional effects of Co.

4 Conclusions

In summary, we prepared Co–Mo–S alloy thin films with varying Co content by the thermal sulfurization of the sputter deposited Co:Mo alloy thin films and tested their activity in HER. When compared to MoS_2, the Co–Mo–S alloy films exhibit superior HER performance, the Co–Mo–S (3:10) being the most active catalyst among others with an overpotential of 352 mV at 10 mA cm^{-2}, a Tafel slope of 62 mV dec^{-1} as well as good stability in acidic solution. The enhanced catalytic activity of the Co–Mo–S alloy films can be ascribed to four possible reasons: (1) The Co incorporation into the MoS_2 lattice modulates the electronic states of the in-plane sulfur atoms to result in a more favorable ΔG_H, in turn activating the basal plane. (2) The Co induces n-type doping in the MoS_2, improving its charge transport ability. (3) The morphology of the MoS_2 film is modified by the Co, resulting in increased roughness and ECSA. (4) The curvature of the spherical nano-grains observed in the Co–Mo–S alloy films puts a geometrical constraint on the surface atoms, thereby modulating ΔG_H. This study provides an effective strategy to modify the electronic structure of MoS_2 and consequently enhance its catalytic activity in HER.

Supplementary Information The online version contains supplementary material available at https://doi.org/10.1007/s10562-021-03639-z.

Acknowledgements This work was supported by The Scientific and Technological Research Council of Turkey (Grand No. 117M257).

Declarations

Conflict of Interest The authors declare no conflict of interests regarding the publication of this article.

References

1. Hinnemann B, Moses PG, Bonde J, Jørgensen KP, Nielsen JH, Horch S, Chorkendorff I, Nørskov JK (2005) J Am Chem Soc 127:5308–5309
2. Voiry D, Salehi M, Silva R, Fujita T, Chen M, Asefa T, Shenoy VB, Eda G, Chhowalla M (2013) Nano Lett 13:6222–6227
3. Zheng X, Xu J, Yan K, Wang H, Wang Z, Yang S (2014) Chem Mater 26:2344–2353
4. Tang Q, Jiang D (2016) ACS Catal 6:4953–4961
5. Wang H, Lu Z, Xu S, Kong D, Cha JJ, Zheng G, Hsu PC, Yan K, Bradshaw D, Prinz FB, Cui Y (2013) PNAS 110:19701–19706
6. Zhang J, Wu J, Guo H, Chen W, Yuan J, Martinez U, Gupta G, Mohite A, Ajayan PM, Lou J (2017) Adv Mater 29:1701955
7. Jaramillo TF, Jorgensen KP, Bonde J, Nielsen JH, Horch S, Chorkendorff I (2007) Science 317:100–102
8. Li Y, Wang H, Xie L, Liang Y, Hong G, Dai H (2011) J Am Chem Soc 133:7296–7299
9. Wang H, Lu Z, Kong D, Sun J, Hymel TM, Cui Y (2014) ACS Nano 8:4940–4947
10. Ye G, Gong Y, Lin J, Li B, He Y, Pantelides ST, Zhou W, Vajtai R, Ajayan PM (2016) Nano Lett 16:1097–1103
11. Xie J, Zhang H, Li S, Wang R, Sun X, Zhou M, Zhou J, Lou XW, Xie Y (2013) Adv Mater 25:5807–5813
12. Wang Z, Li Q, Xu H, Dahl-Petersen C, Yang Q, Cheng D, Cao D, Besenbacher F, Lauritsen JV, Helveg S, Dong M (2018) Nano Energy 49:634–643
13. Wang D, Wang Z, Wang C, Zhou P, Wu Z, Liu Z (2013) Electrochem Commun 34:219–222
14. Geng X, Wu W, Li N, Sun W, Armstrong J, Al-hilo A, Brozak M, Cui J, Chen TP (2014) Adv Func Mater 24:6123–6129
15. Zhao Y, Xie X, Zhang J, Liu H, Ahn HJ, Sun K, Wang G (2015) Eur J Chem 21:15908–15913
16. Luo R, Luo M, Wang Z, Liu P, Song S, Wang X, Chen M (2019) Nanoscale 11:7123–7128
17. Yoshimura A, Koratkar N, Meunier V (2020) Nano Express 1:010008
18. Wang C (2019) Int J Electrochem Sci 14:9805–9814
19. Wang Y, Sun W, Ling X, Shi X, Li L, Deng Y, An C, Han X (2019) Eur. J. Chem. 2019 04238.
20. Xue J-Y, Li F-L, Zhao Z-Y, Li C, Ni CY, Gu HW, Young DJ, Lang JP (2019) Inorg Chem 58:11202–11209
21. Li Q, Liu W, Xiao L, Chen X, Xu X (2021) Mater Lett 285:129196
22. Kuru C, Alaf M, Simsek YE (2021) Catal. Lett.
23. Dai X, Du K, Li Z, Liu M, Ma Y, Sun H, Zhang X, Yang Y (2015) ACS Appl Mater Interfaces 7:27242–27253
24. Lin C, Gao Z, Jin J (2018) Chem Sus Chem 11:2114–2123
25. Ambrosi A, Pumera M (2018) Eur J Chem 24:18551–18555
26. Miao J, Xiao F-X, Yang HB, Khoo SY, Chen J, Fan Z, Hsu YY, Chen HM, Zhang H, Liu B (2015) Sci. Adv. 1:e1500259
27. Li Y, Yin J, An L, Lu M, Sun K, Zhao YQ, Gao D, Cheng F, Xi P (2018) Small 14:1801070
28. Chen L, Zhang Y, Wang H, Wang Y, Li D, Duan C (2018) Nanoscale 10:21019–21024
29. Yang Y, Fei H, Ruan G, Xiang C, Tour JM (2014) Adv Mater 26:8163–8168
30. Li H, Zhang Q, Yap CCR, Tay BK, Edwin TH, Olivier A, Baillargeat D (2012) Adv Func Mater 22:1385–1390
31. Ryu M-Y, Jang H-K, Lee KJ, Piao M, Ko SP, Shin M, Huh J, Kim GT (2017) Phys Chem Chem Phys 19:13133–13139
32. Sahoo S, Gaur AP, Ahmadi M, Guinel MJF, Katiyar RS (2013) J Phys Chem C 117:9042–9047
33. Kong D, Wang H, Cha JJ, Pasta M, Koski KJ, Yao J, Cui Y (2013) Nano Lett 13:1341–1347
34. Huang X, Zeng Z, Zhang H (2013) Chem Soc Rev 42:1934
35. Ghosh S, Azad UP, Singh AK, Singh AK, Prakash R (2017) Chem Select 2:11590–11598
36. Kibsgaard J, Chen Z, Reinecke BN, Jaramillo TF (2012) Nat Mater 11:963–969
37. Xu C, Peng S, Tan C, Ang H, Tan H, Zhang H, Yan Q (2014) J Mater Chem A 2:5597–5601
38. Yu J, Cao Q, Feng B, Li C, Liu J, Clark JK, Delaunay JJ (2018) Nano Res 11:4323–4332

Authors and Affiliations

Cihan Kuru[1,3] · Mirac Alaf[1,3] · Yunus E. Simsek[2,3] · Ubeyd Tocoglu[4]

✉ Cihan Kuru
cihan.kuru@bilecik.edu.tr

[1] Department of Metallurgical and Materials Engineering, Bilecik Seyh Edebali University, Bilecik 11230, Turkey

[2] Department of Chemical Engineering, Bilecik Seyh Edebali University, Bilecik 11230, Turkey

[3] Biotechnology Application and Research Centre, Bilecik Seyh Edebali University, Bilecik 11230, Turkey

[4] Department of Metallurgical and Materials Engineering, Sakarya University, Sakarya 54050, Turkey